atmosphere

Article

Regional Warming Event in Winter on the Ross Ice Shelf, Antarctica as Observed by UW-Madison Automatic Weather Stations

David E. Mikolajczyk [1,*], Jonathan E. Martin [2], Linda M. Keller[2] and Matthew A. Lazzara [1,3]

[1] Antarctic Meteorological Research and Data Center, Space Science and Engineering Center, University of Wisconsin-Madison, Madison, WI, USA 53706; david.mikolajczyk@ssec.wisc.edu, mattl@ssec.wisc.edu
[2] Atmospheric and Oceanic Sciences Department, University of Wisconsin-Madison, Madison WI, USA 53706; jemarti1@wisc.edu, lmkeller@wisc.edu
[3] Department of Physical Sciences, School of Engineering, Science, and Mathematics, Madison Area Technical College, Madison, WI, USA 53704; mlazzara@madisoncollege.edu
* Correspondence: david.mikolajczyk@ssec.wisc.edu

Abstract: From 12-15 July 2007, a regional warming event in winter (RWEW) on the Ross Ice Shelf (RIS) was observed by the University of Wisconsin-Madison (UW-Madison) Automatic Weather Station (AWS) network. A warming event is defined as an AWS observing an increase in temperature of 30° C or greater in five days or fewer. Preceding this RWEW, a stationary low in the Ross Sea and ridge downstream in the Amundsen Sea built up a pool of warm air just off the coast and northeast of the RIS. Calm conditions over the RIS led to cooling surface temperatures. A barotropic cyclonic disturbance progressed from the Adelie Land coast and merged with the stationary cyclone in the Ross Sea, after which it deepened and progressed southward towards the RIS. The approaching cyclone eroded the cold pool and initiated the RWEW with a warm front that brought warm air advection, cloud cover, and increased wind speeds. Fourteen AWS observed warming events during this RWEW. This study investigates how the atmospheric environment evolved throughout the RWEW in the context of known circulation regimes. This study also compares AWS observations during the RWEW to their climatological means to investigate the significance of the temperature and wind changes because of this RWEW. Due to their spread across the RIS and varying topographical influences, several mechanisms led to the warming events. Warm air advection alone was not enough to sustain a warming event of this magnitude, suggesting the need to understand how complex interactions can lead to surface warming over the RIS and the Antarctic.

Keywords: Warming; Temperature; Antarctic; Cyclone; Front; Observations

Citation: To be added by editorial staff during production.

Academic Editor: Firstname Lastname

Received: date
Revised: date
Accepted: date
Published: date

1. Introduction

A regional warming event in winter (RWEW) was observed from 12-15 July 2007 on the Ross Ice Shelf (RIS), Antarctica by the University of Wisconsin-Madison (UW-Madison) Automatic Weather Station (AWS) network. AWS temperature observations showed dramatic and steady warming in a short period of time. For this study, a warming event is defined as an AWS observing an increase in temperature of greater than 30° C in five or fewer days. To be a regional warming event, more than one AWS needs to observe such a warming event in the same region of Antarctica at approximately the same time. For this RWEW, a warming event was observed by 14 AWSs on the RIS. The warming began at different times at the different AWSs, and for some stations the temperature increase was at different rates, but the event essentially spanned the entire RIS. This study examines how the meteorological environment preceding the RWEW, and subsequent development throughout, led to numerous RIS AWSs observing the warming.

The Antarctic continent is comprised almost entirely of a deep layer of ice and snow and is divided into two broad regions: East Antarctica and West Antarctica (Fig. 1a, b). Refer to Fig. 1b for regions of the Antarctic referenced in this study. The RIS is a flat, floating ice shelf with elevations near sea level and an area approximately the size of France. It is formed by glacier ice flowing from the East Antarctic Plateau to the west and south and from West Antarctica to the east. The RIS is bordered on its west and south by the relatively steep Transantarctic Mountains; on its east by the gentler-sloping West Antarctic Plateau; and on its north by the Ross Sea.

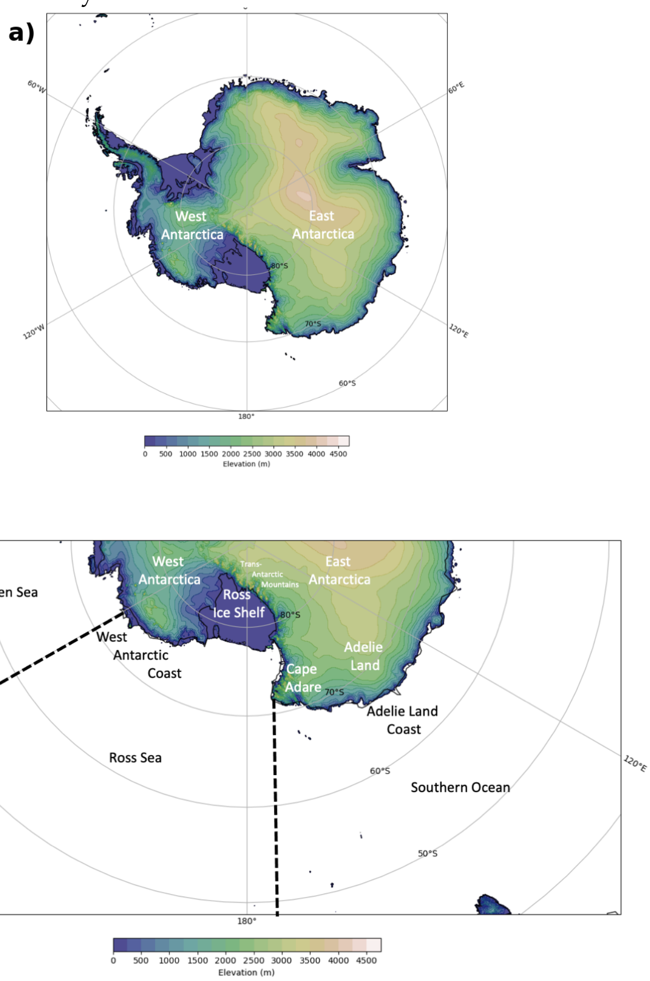

Figure 1: a) The topography of Antarctica (m). Contours are every 250 m. b) Labels of regions referenced in this study. The black dashed lines separate the Southern Ocean, Ross Sea, and Amundsen Sea.

The UW-Madison has managed an AWS network in Antarctica since 1980 [1]. These AWS observe near-surface meteorological variables such as temperature, pressure, and wind speed and direction. Over the years, this AWS network has grown to include upwards of 60 AWS, approximately one-third of which are located throughout the RIS. In 2007, there were 19 AWS on the RIS or near Ross Island (Fig. 2), with the majority in the northwest portion of the region. Despite this local concentration of stations, the distribution of the RIS AWS still captures the different influences of topography on temperature and wind regimes.

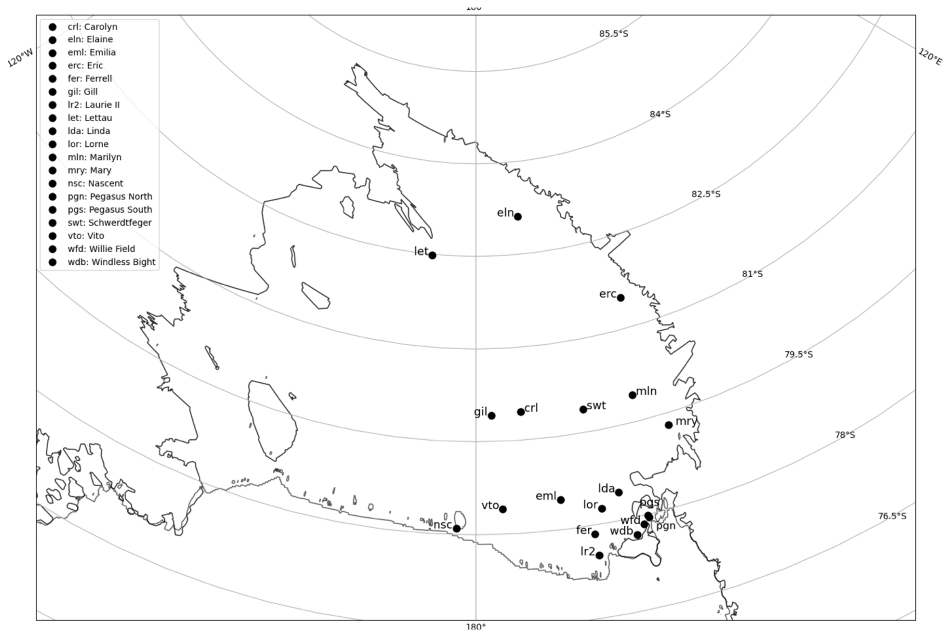

Figure 2: All AWS installed on the Ross Ice Shelf in 2007.

One noted feature of the Antarctic climate, at odds with the rapid warming observed in the RWEW for this study, is the coreless winter, where monthly mean temperatures drop sharply in the autumn followed by relatively uniform, cold temperatures until spring [2-6]. [5] note that, in winter, there is a slight increase in the annual mean temperature cycle at D-10 AWS, near the coast. They denote this as a bump in the second harmonic of the annual temperature, a feature noted similarly at the South Pole in [6]. This slight increase in wintertime temperature has also led to the characterization of a "first-" and "second-winter", during which the Antarctic temperature trends at certain sites can be split into two regimes, the former being slightly warmer than the latter [6-7].

Antarctic temperature regimes vary depending on various factors. [7] conducted a climatology of UW-Madison AWS on the RIS, analyzing temperature, pressure, and wind speed and direction observations. They separated the RIS into three representative regions: central, coastal, and along the Transantarctic Mountains. AWS in the central RIS were found to observe the coldest mean temperatures and the lowest mean resultant (vectorial average) wind speeds. The warmest mean temperatures and highest mean resultant wind speeds were observed at AWS along the Transantarctic Mountains, and the lowest mean pressures were observed at AWS in the coastal region.

There are features of the large-scale Antarctic atmospheric circulation that can affect smaller-scale atmospheric features over the continent. On the East Antarctic Plateau, studies have found that the main cause for rapid surface warming is a synoptic-scale blocking high at upper-levels formed at the leading edge of a stationary Rossby wave train that propagated from lower latitudes and along the Southern Ocean, leading to poleward flow of warm air [8-9]. In the West Antarctic and RIS regions, the Amundsen-Bellingshausen Seas Low (ABSL) is a climatological low-pressure feature in the Amundsen-Bellingshausen Seas region that supports the poleward flow of air [10]. They note that the ABSL shifts westward towards the Ross Sea from summer to winter. This shifts the area of poleward, meridional flow from the Ellsworth Land/Antarctic Peninsula region to the Marie Byrd Land/Siple Coast region.

For the RIS, the synoptic-scale setup leading to rapid warming typically results from the passage of cyclonic disturbances in the Ross Sea [11]. These cyclonic disturbances may originate from a prominent region of cyclogenesis upstream of the RIS off the coast of Adelie Land [12]. The authors in this study investigated how cyclones form off the coast of Adelie Land using output from the Antarctic Mesoscale Prediction System (AMPS) for the years 2003-2005, finding two primary patterns: secondary development and lee cyclogenesis. The former is dependent on enhanced low-level cyclonic vorticity and baroclinicity resulting from an existing synoptic-scale cyclone to the west of Adelie Land, coastal barrier winds, and katabatic winds. The latter occurs on the cyclonic-shear side of the Adelie Land katabatic jet, where a low-level warm potential temperature anomaly sets up a lee trough that propagates eastward off Cape Adare and into the Ross Sea with the arrival of upper-level synoptic-scale forcing.

These synoptic-scale disturbances have complex effects on the atmospheric patterns in the RIS region, mostly owing to the complex topography of the region. One such notable feature is the Ross Ice Shelf air stream (RAS), a prominent feature of the low-level wind field over the RIS [13-14, 11]. These studies have found that the RAS begins at the southern tip of the RIS due to a confluence of drainage flow from the East and West Antarctic plateaus. Synoptic-scale disturbances can enhance the pressure gradient over the RIS along the Transantarctic Mountains, thereby strengthening the RAS. [15] found that there is strong seasonality to the RAS, with it being more common in the winter. Additionally, its strength is dependent on the position of the cyclone in the Ross Sea. By examining the meteorological environment before, during, and after the RWEW in this study, the climatological temperature, wind, and cyclone patterns in and around the RIS can be used to understand the mechanisms by which such a rapid and large-scale surface temperature warming occurred.

For the event in this study, AWS observational data (temperature, pressure, wind speed and direction) from the 14 AWS that observed a warming event are studied. Figure 3 shows temperature observations at Schwerdtfeger, which observed a warming event from 02:30 UTC 13 July to 13:50 UTC 15 July. The preceding synoptic environment consisted of a stationary surface cyclone in the Ross Sea, a ridge upstream in the Amundsen Sea, and a strong zonally oriented baroclinic zone. A cyclone propagating off Cape Adare merged with the existing surface cyclone, reorienting the baroclinic zone to advect warm air towards the RIS. The wind field of the RIS was modified due to the approaching cyclone, enhancing the effects of warming along the Transantarctic Mountains. The European Centre for Medium Range Weather Forecasts (ECMWF) Reanalysis Interim (ERA-I) [16] and version 5 (ERA5) [17] data are used to assess the upper- and lower-level synoptic setup to this event to investigate how this warming event compared to others in the RIS and the Antarctic. Section 2 describes the data and methodology used for this study, including a discussion of the AWS, reanalysis, and satellite data. Section 3 consists of a case study analysis of the 12-15 July 2007 RWEW over the RIS. Section 4 consists of a discussion of this case study RWEW, how it relates to previously documented warming events in the Antarctic, and the roles of turbulent mixing, warm air advection, and cloud cover contributing to this RWEW. Section 5 outlines future work, including investigation of the large-scale influences on this warming event and how that can be used to understand previous and future warming events in the Antarctic.

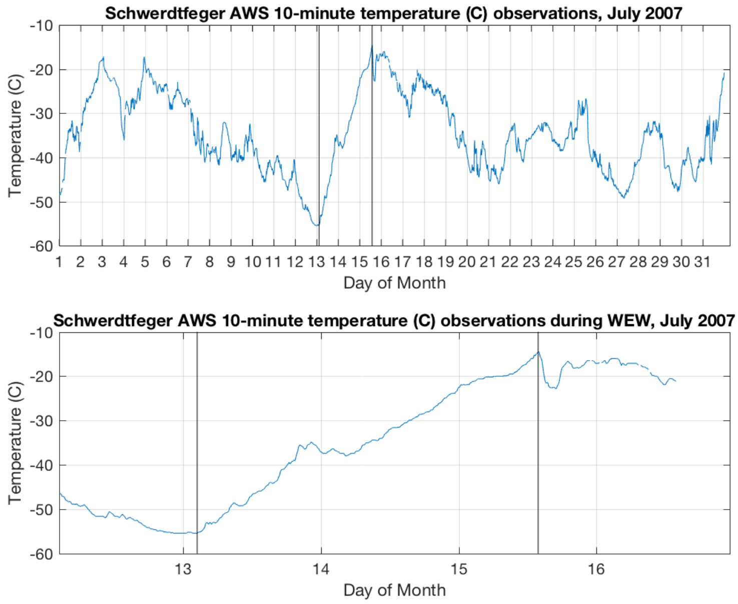

Figure 3: Temperature observations at Schwerdtfeger for July 2007 (top) and 12-16 July 2007 (bottom). The black vertical lines denote the beginning and ending of the warming event.

2. Materials and Methods

Observational data from the UW-Madison AWS network were examined to determine whether a warming event occurred in the study period of 12-15 July 2007. These data are 10-minute, quality-controlled observations (q10) that include temperature, pressure, wind speed, and wind direction. The beginning and ending of the warming events were subjectively determined. When there was a temperature increase of 30° C or greater in five or fewer days, the beginning of that temperature increase was chosen based on when the trend switched from neutral or negative to positive. The ending of the event was chosen when the trend switched from positive to neutral or negative. There were 19 AWSs installed on the RIS or in the Ross Island region during the time of this RWEW. It was determined that 14 distinct AWSs observed this warming event. If an AWS was missing observational data during the study period of interest and hence did not have a continuous enough data set, it is not included in this study. Each of the 14 AWS observing warming had quality-controlled data available that were nearly uninterrupted throughout the event. Table 1 lists each AWS that observed the warming, its start and end times, and the observational data at the beginning and end of the warming. For computing climatological statistics for the 14 AWSs, all available 3-hourly quality-controlled data in the period 1991-2020 were used. The 3-hourly time resolution was chosen because there is a more complete record of quality-controlled data at this increment than at the 10-minute resolution. For comparing AWS data to ERA5 reanalysis data (as we will do in subsequent portions of the analysis), 1-hourly quality-controlled AWS data were used to match ERA5's time resolution.

For the synoptic meteorological analysis of the RWEW, ERA-I and ERA5 reanalysis output, CloudSat and CALIPSO satellite retrievals, and infrared satellite composite imagery were used. The ERA-I reanalysis data are based on a gridded dataset of recorded climate observations at 0.7° x 0.7° spatial resolution and 6-hourly temporal resolution [16]. ERA5 reanalysis data are at 0.25° x 0.25° spatial resolution (31 km), 1-hourly temporal resolution, and are based on the Integrated Forecasting System Cy41r2 and observational data assimilation to model the atmosphere [17]**.** [18] compared ERA5 and ERA-I reanalysis output to AWS data in the southern Antarctic Peninsula and Ellsworth Land regions and found similar results in ERA5 surface air temperature performance. The authors also found ERA5 accurately captured the surface wind regime above 1000 m, but coastal regions exhibited a wind bias of -1.48 m s^{-1}. Since the Ross Sea borders the RIS, and RIS surface elevations are near sea level, it can be considered a coastal region, and these ERA5 wind biases will be considered when using ERA5 10-m wind data.

To further test the validity of ERA5 reanalysis data for this study, correlations between AWS observations and ERA5 data were calculated. A nearest-neighbor approach was employed between hourly AWS observations and ERA5 data for temperature, pressure, and wind speed. The period examined was from 00 UTC 10 July through 23 UTC 17 July to capture the state of the atmosphere before, during, and after the RWEW (Fig. 4). Temperature differences between the AWS observations and ERA5 were generally within +/-4° C though sometimes reached +/-8° C. ERA5 mean sea level pressure values were greater than AWS pressure observations at each site, typically by approximately 5-10 hPa. During each distinct warming event, correlations were calculated between hourly AWS observations and hourly ERA5 data for temperature, pressure, and wind speed. Strong correlations were found for temperature (most with an r^2 value greater than or equal to 0.92) and pressure (most with an r^2 value greater than or equal to 0.99). For wind speed, weaker correlations were found between AWS wind speed observations and ERA5 10-m wind speed, with about half of the r^2 values between 0.40 and 0.80. Given these correlation results and considering previous work on the validity of ERA5 2-m temperatures, the ERA5 2-m temperatures were considered to accurately represent the magnitude and trends of temperature. The ERA5 mean sea level pressure accurately represents the pressure trends though they exhibit a positive bias. Since the wind speeds were at two different levels (approximately 2-m for AWS observations, 10-m for ERA5) and the correlations were satisfactory, the ERA5 10-m winds were deemed to fairly represent the near-surface wind field during the RWEW.

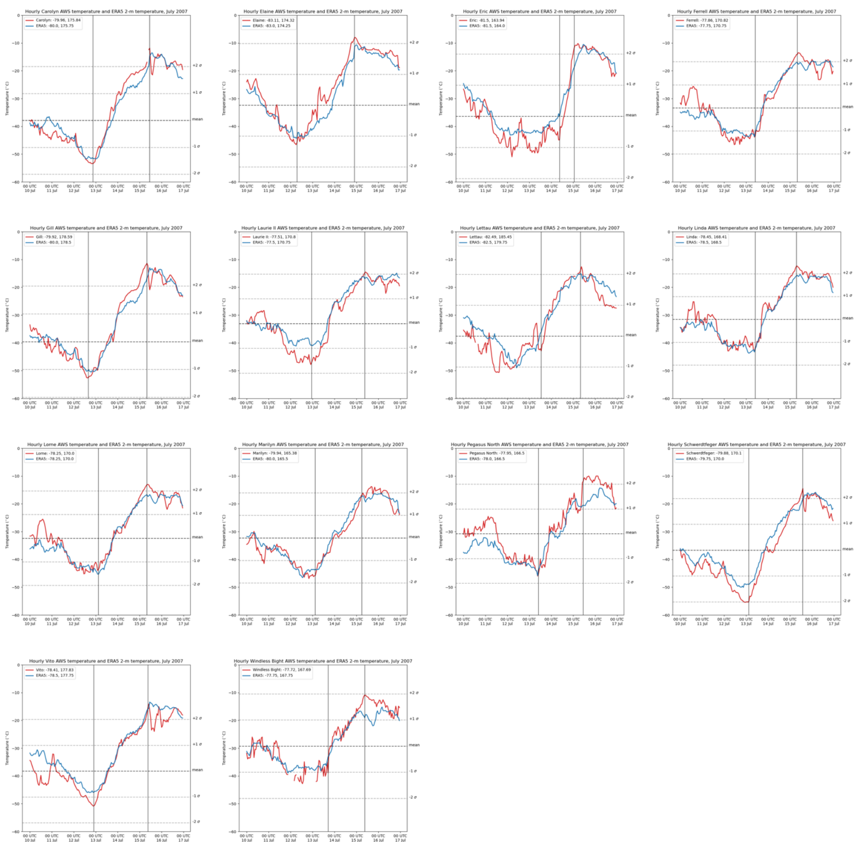

Figure 4: Hourly temperatures of AWS observations (red) and ERA5 2-m temperatures (blue) (° C) from 10 through 17 July 2007, with separate plots for each of the 14 AWS observing warming. Black vertical lines denote the beginning and ending of the warming events. Horizontal dashed lines indicate the respective AWS climatological July monthly mean temperature and +/-1 and +/-2 standard

deviations from the mean. The legend includes the AWS coordinates and the ERA5 coordinates of the nearest grid cell.

The following ERA-I reanalysis output data were used to study the synoptic-scale evolution of this RWEW: 300-hPa geopotential height and wind; 500-hPa geopotential height, temperature, wind, and relative vorticity; 850-hPa geopotential height, temperature, wind, specific humidity, and relative vorticity; and mean sea level pressure, 10-m winds, and 2-m temperature. ERA5 2-m temperatures and 10-m winds were used. Infrared satellite composite imagery over the Antarctic region from the Antarctic Meteorological Research Center (AMRC) [19-20] were used to determine locations of surface low pressure systems and cloud signatures. During the study period, the temporal resolution for this imagery is 3-hourly; the spatial resolution is 5 km nominal resolution at 60° South.

Satellite data retrievals from CloudSat and Cloud-Aerosol Lidar and Infrared Pathfinder (CALIPSO) [21], part of the National Aeronautics and Space Administration (NASA) Afternoon-Train (A-Train) group of polar-orbiting satellites, were used to assess the cloud characteristics and radiative flux properties above the RIS and surrounding region for this RWEW. CloudSat uses its 94-GHz Cloud Profiling Radar (CPR) to provide information about cloud structure. Reflectivity (dBZ) from the 2B-GEOPROF R05 product [22] were used. Output examined were cloud phase (liquid, mixed, or iced) from the 2B-CLDCLASS-lidar R05 product [23] and downwelling longwave (W m^{-2}), and bottom of the atmosphere longwave cloud radiative effect (W m^{-2}) from the 2B-FLXHR-LIDAR [24]. ECMWF temperature and land surface type were plotted to supplement analysis of the satellite observations along the satellite pass. The ECMWF temperatures are a product from the ECMWF-AUX dataset, which is an intermediate product for the CloudSat Data Processing Center (DPC) that contains the set of ancillary ECMWF state variable data interpolated to each CloudSat cloud profiling radar bin and the input data is obtained from the AN-ECMWF dataset provided by the ECMWF [25]. The time stamps for CloudSat/CALIPSO plots used in this study are from the midpoint of the respective swath path.

3. Results

3.1. RWEW Case Study: AWS Observations

From 6:20 UTC 12 July 2007 through 14:40 UTC 15 July 2007, 14 AWS on the RIS observed warming events. Figure 5a shows the location of each AWS and timing of warming event onset, with the colors corresponding to when the warming began for each AWS. Figure 5b shows the topographical elevation of Antarctica and the names of geographical features referenced throughout the remainder of this paper. The first AWS to observe a warming event was Elaine (eln), on the southern end of the RIS near the Transantarctic Mountains, starting at 6:20 UTC 12 July (Table 1). Throughout 12 July, AWS farther north on the RIS began observing warming (Gill (gil), Carolyn (crl), Vito (vto), Laurie II (lr2)). Early on 13 July, the several AWSs near Ross Island, at the northwest corner of the RIS, began observing warming (Schwerdtfeger (swt), Lorne (lor), Marilyn (mln), Ferrell (fer), Pegasus North (pgn), Linda (lda), Windless Bight (wdb)). Midday on 13 July, Lettau (let) began observing warming. The last AWS to begin observing warming was Eric (erc), near the Transantarctic Mountains, starting at 8:50 UTC 14 July. The warming events for all AWS ended on 15 July, except for Elaine, which ended on 14 July. Figure 6 shows AWS observation plots of temperature, pressure, wind speed, and wind direction, for the duration of the warming event. For each AWS, as the temperature increased throughout the event, the pressure decreased. For wind speeds at most AWSs, as the warming event progressed, the wind speeds increased through the middle of the event and then plateaued; for others, the speed did not change much throughout. Wind directions throughout the warming events were steady, particularly for AWS with high wind speeds. There were negative correlations between temperature and pressure for all

AWS (not shown), and all except Elaine showed a strong negative correlation of greater than -0.90. This suggests a strong relation to the arrival of a low-pressure system coincident with warming. The correlations to wind speed were more varied, however. This could be due to several factors, including varying influence from the larger-scale synoptic environment, varying topographical influences, and instrumentation malfunction.

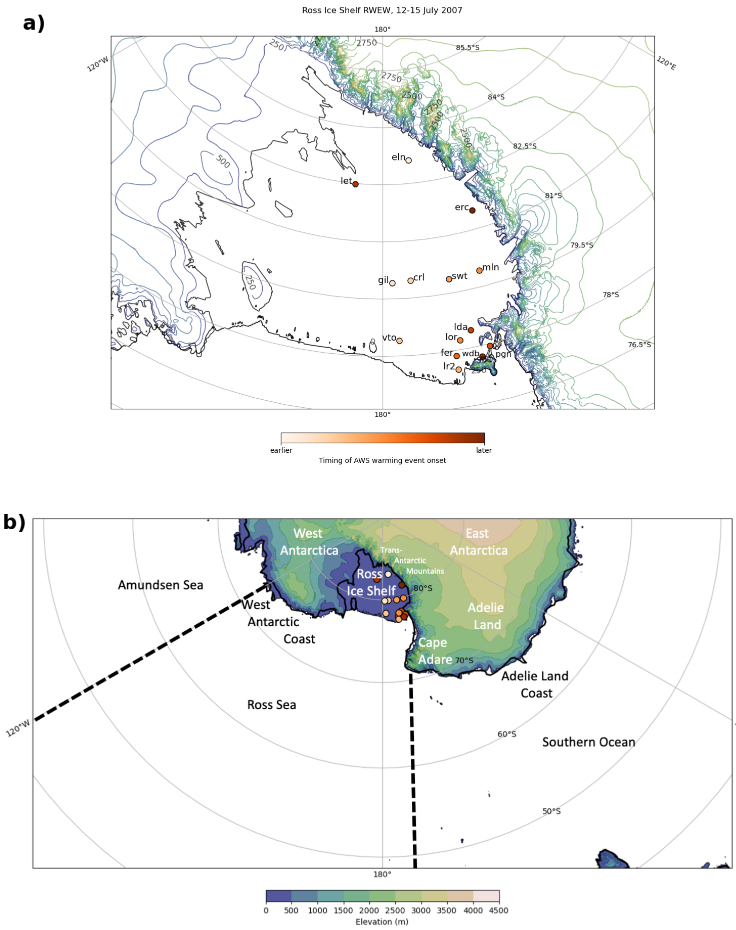

Figure 5: a) Map of the RIS with each AWS location color-coded based on onset of warming event, and topographical contours every 250 m and color-coded as shown in the legend in b), and b) as in Fig. 1b, but with the AWS locations included, color-coded as in a).

Table 1. Locations and observational data for each AWS observing a warming event in the RWEW, listed in alphabetical order.

AWS	ID	Lati-tude	Longi-tude	Time, start (UTC)	Time, end (UTC)	Temp, start (°C)	Temp, end (°C)	Pressure, start (hPa)	Pressure, end (hPa)
Carolyn	crl	-79.964	175.842	20:20 12 Jul	11:00 15 Jul	-53.6	-11.9	990.0	974.3
Elaine	eln	-83.111	174.316	6:10 12 Jul	22:10 14 Jul	-47.2	-7.9	999.1	978.2

Eric	erc	-81.504	163.939	8:40 14 Jul	1:30 15 Jul	-45.4	-10.8	NA	977.4
Ferrell	fer	-77.860	170.819	9:20 13 Jul	8:30 15 Jul	-44.5	-13.5	1003.5	973.9
Gill	gil	-79.922	-178.586	15:40 12 Jul	8:20 15 Jul	-52.8	-11.1	999.3	975.9
Laurie II	lr2	-77.509	170.797	22:10 12 Jul	9:40 15 Jul	-48.0	-14.2	1004.3	974.9
Lettau	let	-82.486	-174.553	12:50 13 Jul	8:40 15 Jul	-43.1	-12.4	1003.4	987.5
Linda	lda	-78.453	168.410	9:40 13 Jul	6:50 15 Jul	-42.9	-12.4	1005.1	974.6
Lorne	lor	-78.250	170.000	2:40 13 Jul	8:10 15 Jul	-44.0	-13.0	1004.6	974.0
Marilyn	mln	-79.935	165.378	2:40 13 Jul	6:30 15 Jul	-46.4	-15.6	1002.8	973.6
Pegasus North	pgn	-77.957	166.515	9:20 13 Jul	11:30 15 Jul	-46.0	-10.0	1010.7	980.9
Schwerdtfeger	swt	-79.875	170.105	2:30 13 Jul	13:50 15 Jul	-55.4	-14.5	1000.9	975.8
Vito	vto	-78.501	177.753	21:50 12 Jul	9:30 15 Jul	-51.0	-13.6	1002.7	975.3
Windless Bight	wdb	-77.723	167.692	16:50 13 Jul	9:00 15 Jul	-41.2	-10.9	1002.1	977.0

271

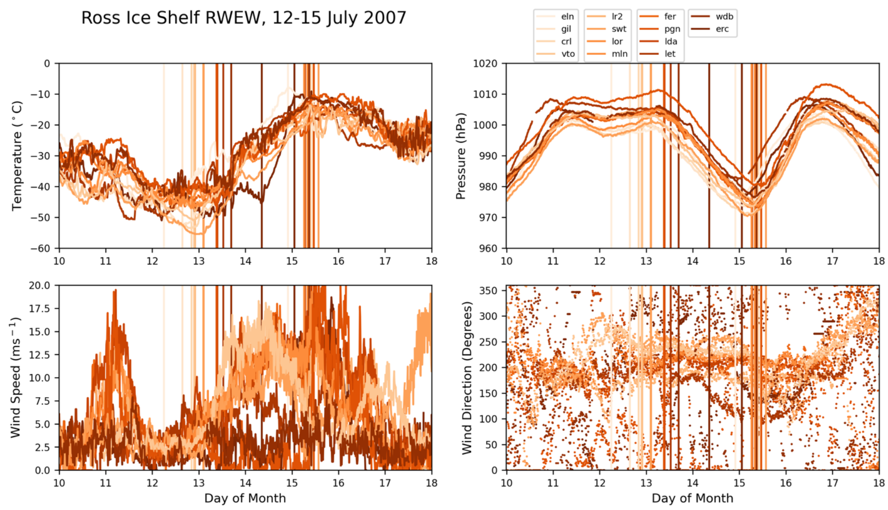

Figure 6: AWS observations from 10-17 July 2007 of temperature (° C) (upper left), pressure (hPa) (upper right), wind speed (m s^{-1}) (lower left), and wind direction (degrees) (lower right). All data plotted are color-coded as in Fig. 5a.

3.2. RWEW Case Study: Synoptic Assessment

3.2.1. Two days prior to warming event onset

For the two days prior to the beginning of the RWEW, from 00 UTC 10 July to 12 UTC 12 July, collocated geopotential height minima at 300, 500, and 850 hPa and a mean sea level pressure minimum were situated in the northeast Ross Sea with strong northerly flow downstream (Fig. 7a, b, c, and d). At 300 hPa (Fig. 7a), a large geopotential height gradient extended from the Ross Sea height minimum southeastward to the West Antarctic coast where a local wind speed maximum, or jet streak, was located. At lower levels in this same region, a large temperature gradient was established. This was due to warm air advection from the northerly flow, as the wind barbs at 500 and 850 hPa were oriented nearly perpendicularly to isotherms just southeast of the low (Fig. 7b and c).

Near the surface (Fig. 7d), the warm air advection was east and southeast of the Ross Sea low. The isotherms indicate the baroclinic zone at 500 hPa ranged from -28° C on the northern edge to -40° C on the southern edge; at 850 hPa it ranged from 0° C to -20° C; and at the surface it ranged from 0° C to -16° C. The 850-hPa relative vorticity indicates two cyclonic relative vorticity minima within the Ross Sea geopotential height minimum, the southern of which extended along the baroclinic zone. A distinct trough axis in mean sea level pressure was at this same location. At the southern tip of the RIS, there was another collocated upper-level height minimum and surface low. A collocated local 850-hPa minimum in cyclonic vorticity suggests a robust cyclonic circulation. The broad influence of this cyclonic circulation can be seen at 300 and 500 hPa, with the northern portion of this low providing a barrier upon which the northerly flow in the Ross Sea was deflected southeastward. This limited the southward extent of the baroclinic zone in the Ross Sea.

Upstream of the Ross Sea low in the Southern Ocean, slight curvature in the flow was evident in the 300- and 500-hPa geopotential height fields along the Adelie Land coast. A 300-hPa ridge with a jet streak on the ridge axis was just off the coast of Cape Adare. A weak trough at those levels was just upstream of that ridge. At 850 hPa and the surface, no such ridging was evident but there was a collocated trough and a zonally elongated low, just north of the Adelie Land Coast. A tight baroclinic zone extended from the elongated low eastward towards the southern portion of the Ross Sea cyclone. This baroclinic zone was less evident at 850 hPa and essentially nonexistent at 500 hPa.

In the Ross Sea, the infrared satellite composite image (Fig. 7e) shows a comma shape of bright white, high-altitude clouds associated with the Ross Sea cyclone. These high clouds also extended southeastward towards the West Antarctic coast in the region of the baroclinic zone. Over the southern Ross Sea and RIS, there were no major cloud signatures, indicating either clear skies or thin, low clouds. Since this is infrared satellite imagery, and there was sea ice, the ice shelf, and continental ice in the region, it can be difficult to distinguish low clouds from the surface as the temperatures of the clouds and surface may be identical. Upstream in the Southern Ocean off the Adelie Land Coast, there was a somewhat organized comma-shaped cloud feature associated with the cyclonic disturbance in this region. Atmospheric conditions at the surface were generally calm over the RIS (Fig. 7f) with 10-m wind barbs indicating low to calm wind speeds, particularly over the western RIS where the AWS were located. AWS temperature observations were generally in the low to mid -30°s C except for Elaine and Eric along the Transantarctic Mountains, which were in the mid -20°s C.

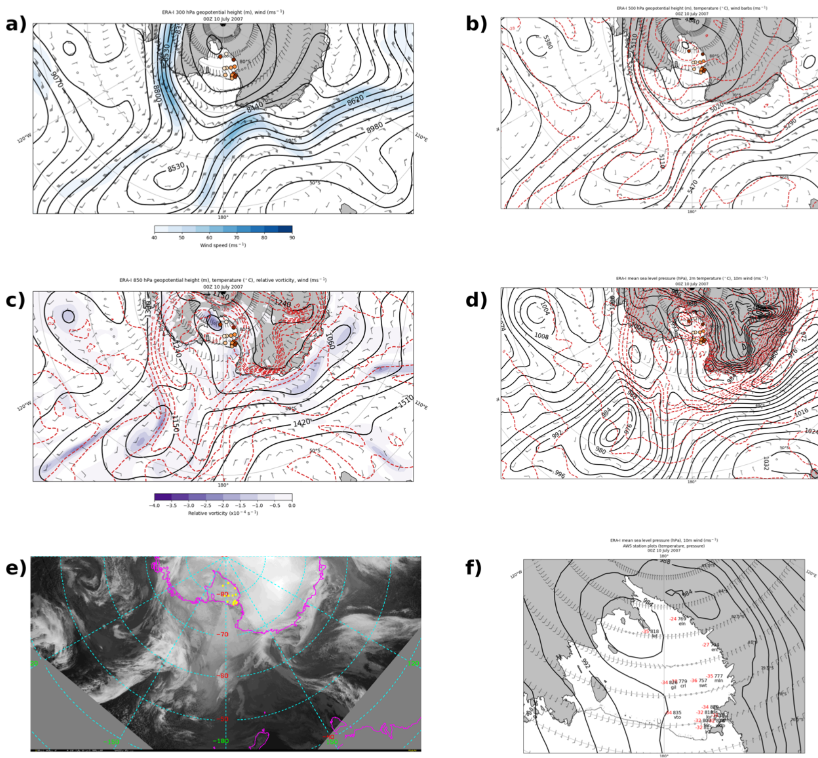

Figure 7: ERA-I 00 UTC 10 July a) 300-hPa geopotential height (m) (black contours), wind speed (m s^{-1}) (fill contours every 5 m s^{-1} from 40 to 90 m s^{-1}), wind barbs (m s^{-1}); b) 500-hPa geopotential height (m) (black contours), temperature (° C) (dashed red contours), wind barbs (m s^{-1}); c) 850-hPa geopotential height (m) (black contours), temperature (° C) (dashed red contours), relative vorticity (10^{-4} s^{-1}) (fill contours from -4 to 0 every 0.5), wind barbs (m s^{-1}); d) mean sea level pressure (hPa) (black contours), 2-m temperature (° C) (dashed red contours), 10-m wind barbs (m s^{-1}); e) infrared satellite composite image with yellow dots denoting AWS locations; f) mean sea level pressure (hPa) (black contours), 10-m wind barbs (m s^{-1}), station plots of AWS observations of temperature (° C, red) in upper left and pressure in upper right where the leading two digits are dropped if the pressure is greater than or equal to 1000 hPa and the leading first digit is dropped if the pressure is less than 1000 hPa. For a)-d), geopotential heights are contoured every 90 m, temperatures are contoured every 4° C, and AWS are plotted as in Fig. 5a.

At 00 UTC 12 July, approximately 6 hours before the first warming event began at Elaine, the northern Ross Sea disturbance became more organized. At 300 hPa, the geopotential height minimum deepened to sub-8440 m, the 500-hPa geopotential height minimum deepened to sub-5020 m and became more organized, the 850-hPa geopotential height minimum deepened to sub-1060 m with a local minimum in cyclonic relative vorticity, and the surface disturbance deepened to sub-968 hPa. Collectively, this disturbance moved slightly southward towards the RIS. At all levels, northerly to northeasterly flow remained downstream as the downstream ridge only progressed slightly eastward in the

Amundsen Sea. At 300 hPa, the wind maximum over the West Antarctic Coast and West Antarctica continued to decrease in magnitude as the ridge building in the Ross Sea continued south of the disturbance. At 500 hPa, with the ridge progressing slightly eastward in the Amundsen Sea, the warm air advection over West Antarctica decreased as the baroclinic zone progressed over West Antarctica. At 850 hPa, the baroclinic zone just south of the disturbance in the northern Ross Sea, with a temperature range of -4° C to -20° C, slightly increased in magnitude. The geographic extent decreased as the warm air advection continued and the atmosphere cooled in the southern Ross Sea. The surface baroclinic zone remained approximately stationary, reaching from the southern portion of the Ross Sea cyclone southeast to the West Antarctic Coast.

Upstream in the Southern Ocean, the cyclonic disturbance progressed eastward and was located to the north of Cape Adare. It weakened slightly as the sea level pressure minimum increased to sub-984 hPa and the cyclonic relative vorticity decreased slightly. The 850-hPa and surface baroclinic zones decreased in magnitude but still extended from the cyclone eastward towards the Ross Sea disturbance. The IR satellite composite imagery indicates that the cloud signature associated with the Ross Sea disturbance began to resemble a comma shape, suggesting further development of the cyclone. Clouds remained over the West Antarctic Coast and Ross Sea region just south of the cyclone, and the cloud shield extending to the east from the Ross Sea cyclone progressed southward. The cloud signature associated with the cyclone upstream off the coast of Cape Adare indicates a large band of high-altitude clouds reached into the Ross Sea region. There were no satellite data at this time over the RIS. The 10-m winds over the RIS indicate light, southerly flow across the majority of the RIS, with calm winds in the northwest portion. The surface pressure was steady as AWS pressure observations did not show much change. AWS temperature observations remained constant or decreased, with some decreasing by ~2-7° C. The coldest observed temperatures were at Lettau and Eric (-48° C).

3.2.2. During warming event

At 12 UTC 12 July, the geopotential height minima at each level as well as the surface low in the Ross Sea progressed slightly southward towards the RIS. The 300-hPa geopotential height minimum remained at sub-8440 m (Fig. 8a), and the ridge building downstream continued, with the ridge extended south of the height minimum. Over the RIS, a local 300-hPa geopotential height minimum remained, with the jet streak likewise remaining approximately stationary over West Antarctica. The southward progression of the 500-hPa geopotential height minimum in the Ross Sea led to warm air advection south of the height minimum that moved the baroclinic zone towards the RIS (Fig. 8b). East of Cape Adare in the Ross Sea, the warm air advection also oriented the northern portion of the baroclinic zone meridionally. The 850-hPa geopotential height minimum decreased to sub-970 m as it progressed south and strengthened, as indicated by the increased cyclonic relative vorticity (Fig. 8c). The baroclinic zone south of the height minimum intensified and progressed slightly southward towards the RIS, with a temperature range of -4° C to -20° C. It was still oriented northwest-to-southeast as it extended to the West Antarctic Coast. The surface cyclone deepened to sub-960 hPa as it shifted westward in the Ross Sea (Fig. 8d). This deepening and shift acted to deform the baroclinic zone to its south, tightening and rotating the temperature gradient near the cyclone clockwise with the increased pressure gradient and increased wind speed. The portion of this baroclinic zone closest to the West Antarctic Coast increased in strength slightly due to the deepening of the cyclone and the 2-m temperatures cooled over the southern Ross Sea, just north of the RIS.

The cyclone upstream progressed eastward near the far western Ross Sea. The collocated trough axes at 300 and 500 hPa were just north of Cape Adare. The 850-hPa height minimum began to merge with the Ross Sea disturbance, and the cyclonic relative vorticity decreased slightly. The mean sea level pressure field shows the surface cyclone was still distinct at this time and maintained its strength at sub-984 hPa. Its associated baroclinic zone weakened, however, as the temperature gradient decreased. The IR satellite composite image shows a much more well-defined comma-shaped cloud structure associated with the Ross Sea disturbance (Fig. 8e). High clouds extended from the cyclone towards the West Antarctic Coast and began to sweep over the southern Ross Sea. The cloud structure with the upstream cyclone became less organized, as there was no identifiable cyclonic circulation but rather some meridionally-oriented bands of clouds. Over the RIS, the 10-m winds remained southerly and calm, particularly over the western RIS (Fig. 8f). While the warming event began at the southern end of the RIS at Elaine, observing -43° C at this time, other AWS further northwest on the RIS continued to cool, with Gill and Schwerdtfeger temperature observing -51° C. Pressure observations generally remained steady across the RIS.

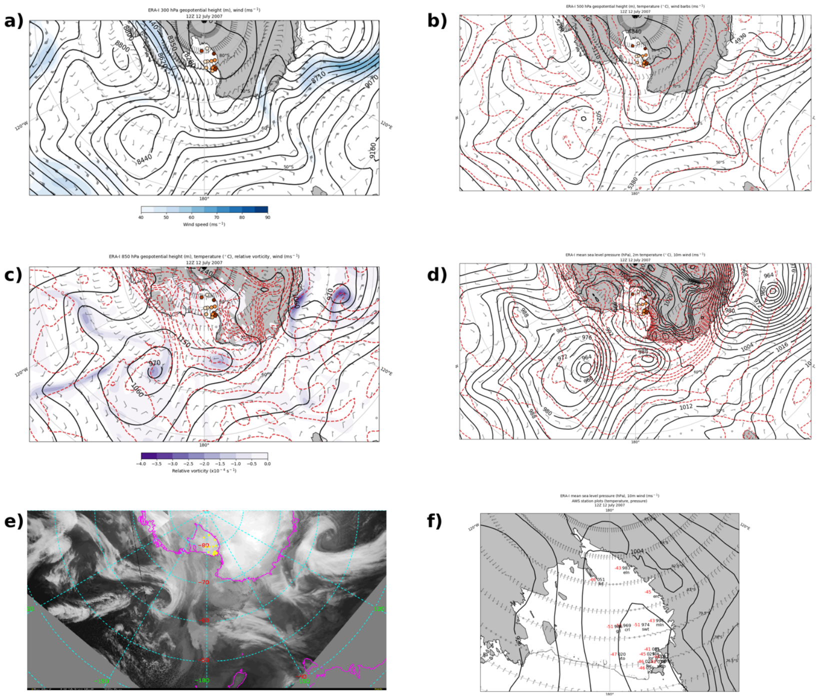

Figure 8: As in Fig. 7 but for 12 UTC 12 July.

At 12 UTC 13 July, a cyclonic circulation encompassed essentially the entire Ross Sea at all levels as the geopotential height minima and surface cyclone continued strengthening. The 300-hPa geopotential height minimum now had a closed-off circulation and was at 8170 m. The ridge downstream progressed further southward over most of West Antarctica and the RIS. The 500-hPa geopotential height minimum in the Ross Sea deepened to 4840 m. The ridge downstream at that level also progressed southward over West Antarctica and the RIS, with warm air advection over the southern Ross Sea and northern RIS rotating the baroclinic zone further clockwise into a meridional orientation. The 850-hPa geopotential height minimum progressed slightly southward and expanded. The band of cyclonic relative vorticity south of the height minimum increased in magnitude as it extended along the trough axis and baroclinic zone. The baroclinic zone now spanned a temperature range of -12° C to -24° C, a slightly smaller temperature range than 12 hours prior. The spatial extent, however, decreased as it progressed southeast and began to move over the eastern RIS. Temperatures over the western RIS began to increase. The surface cyclone weakened slightly as it progressed southward. The temperature gradient increased, and the trough axis progressed south towards the RIS. Temperatures within the baroclinic zone, in the southern Ross Sea, ranged from -4° C to -24° C. The IR satellite composite image shows the cyclone had a less organized cloud structure, though clouds still extended to the northeastern RIS. With the strengthened and approaching cyclone, the mean sea level pressure gradient increased over the RIS, the 10-m wind speeds increased, especially over the eastern RIS, and AWS pressure observations decreased. AWS temperature observations increased at most AWS as the warming events began at Schwerdtfeger, Lorne, Marilyn, Ferrell, Pegasus North, and Linda. Temperatures ranged from -29° C at Elaine to -42° C at Ferrell. The temperature at Eric remained steady at -46° C.

At 00 UTC 14 July, the 300-hPa geopotential height minimum progressed slightly eastward in the Ross Sea as a ridge upstream with a jet streak in the Southern Ocean developed and expanded into the western Ross Sea (Fig. 9a). The ridge downstream remained in the same approximate location. The 500-hPa geopotential height minimum in the Ross Sea deepened to sub-4750 m (Fig. 9b). The ridge downstream continued to build over West Antarctica, with warm air advection over the RIS shifting the baroclinic zone further westward across the RIS (Fig. 9b). The 850-hPa geopotential height minimum was stationary and maintained its strength as the trough axis and baroclinic zone progressed westward over the RIS (Fig. 9c). Although the cyclonic relative vorticity within the trough axis decreased in magnitude, the temperature range remained at -12° C to -24° C. At the surface, the center of the cyclone moved southward and became more circular, maintaining its strength at sub-960 hPa (Fig. 9d). The trough axis and baroclinic zone extending south of the cyclone progressed slightly westward over the southern Ross Sea. The IR satellite composite image was missing data in portions of this region, but the cyclone appears to have regained some more organized cloud structure (Fig. 9e). Throughout the RIS, AWS pressure observations decreased as the mean sea level pressure gradient increased (Fig. 9f). The 10-m winds were southerly over most of the RIS. AWS temperature observations increased as warming events began at Lettau and Windless Bight, while Eric, the final AWS to begin its warming event, began warming at 01:30 UTC 15 July.

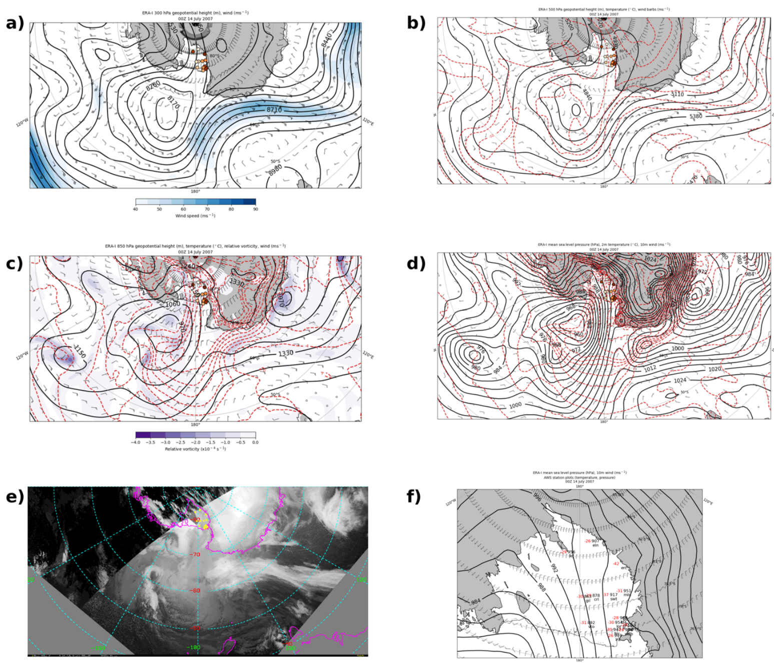

Figure 9: As in Fig. 7 but for 00 UTC 14 July.

At 12 UTC 15 July, the 300-hPa geopotential height minimum in the Ross Sea remained at sub-8170 m but decreased in spatial extent as it progressed southward towards the RIS and elongated meridionally (Fig. 10a). The ridge downstream progressed eastward, decreasing the geopotential height gradient over the RIS. The jet streak to the north progressed further northeastward into the Ross Sea. At 500 hPa, the geopotential height minimum in the southern Ross Sea remained at sub-4840 m but decreased in spatial extent as it became further elongated from northeast-to-southwest (Fig. 10b). Temperatures continued to cool over the RIS, with temperatures in the eastern RIS reaching colder than -40° C. The disturbance at 850 hPa weakened significantly, as the geopotential height minimum increased to sub-1060 m and covered a large area from the southern Ross Sea to the Amundsen Sea (Fig. 10c). The trough over the RIS progressed westward and weakened as the baroclinic zone weakened considerably. There was still a maximum in cyclonic relative vorticity over the northwestern RIS along the Transantarctic Mountains. The surface low in the southern Ross Sea continued weakening to sub-972 hPa, as the secondary low no longer was evident (Fig. 10d). The trough progressed further westward almost entirely across the RIS. The associated 2-m temperature gradient continued to weaken, although temperatures increased over the northwestern RIS. The cyclonic cloud signatures in the southern Ross Sea were much less apparent in the IR satellite composite imagery (Fig. 10e). The cloud cover over the RIS decreased, with the darker and therefore warmer regions suggesting minimal cloudiness to cloud-free conditions. Some higher clouds remained over the western RIS. With the surface trough progressing westward but weakening, the 10-m winds were northerly in the eastern RIS, easterly in the central RIS, and southerly in the western RIS (Fig. 10f). The pressure gradient across the RIS increased slightly, increasing the wind speeds. AWS pressure observations began increasing at most AWS, and AWS temperature observations began to become steady and cool as the warming events ended at Eric, Marilyn, Linda, Lorne, Gill, Ferrell, Lettau, Windless Bight, Vito, Laurie II, Carolyn, and Pegasus North.

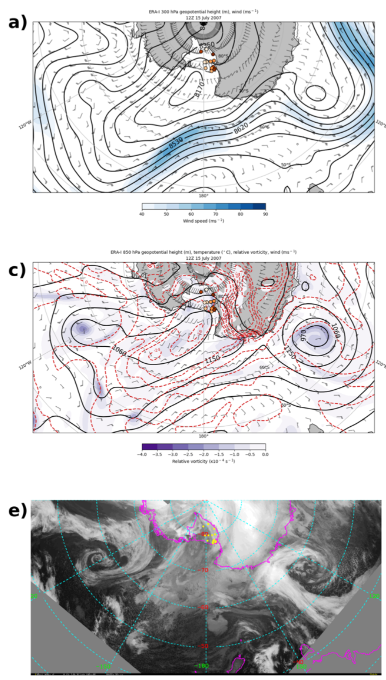

Figure 10: As in Fig. 7 but for 12 UTC 15 July.

3.2.3. After warming event

At 00 UTC 16 July, 10 hours and 10 minutes after the final observed warming event ended, in the south-central Ross Sea there were similarly shaped and positioned geopotential height minima at 300 hPa (Fig. 11a) and 500 hPa (Fig. 11b), while the 850-hPa geopotential height minimum and surface low (Fig. 11c, d) were to their east. The 300-hPa geopotential height minimum weakened to sub-8260 m and elongated northeastward (Fig. 11a). The geopotential height gradient over the RIS weakened slightly, and the jet streak in the Ross Sea to the north of the geopotential height minimum weakened as it progressed further northeastward. A ridge was present in the Amundsen Sea and began to reach over West Antarctica. At 500 hPa, the geopotential height minimum in the Ross Sea weakened to sub-4930 m as it elongated like that at 300 hPa (Fig. 11b). There was not much variation in temperature over the RIS, and they did not change much from 12 hours prior. There was northerly flow and warm air advection upstream off the coast of West Antarctica. At 850 hPa, the center of the geopotential height minimum shifted eastward into the eastern Ross Sea (Fig. 11c). The geopotential height gradient over the RIS weakened slightly, as did the cyclonic relative vorticity near the Transantarctic Mountains. Temperatures remained approximately the same as 12 hours prior. At the surface, the original surface low in the Ross Sea was no longer apparent as a stronger surface low of sub-964 hPa from the northeast in the Amundsen Sea progressed southwest towards the West Antarctic Coast (Fig. 11d). This low was located east of the geopotential height minima at 300 and 500 hPa and in the eastern portion of the 850-hPa geopotential height minimum.

Over the RIS, the 2-m temperature gradient weakened, with generally warmer temperatures in the northern RIS and cooler temperatures in the southern RIS. The western RIS remained generally cloud-free while high clouds moved over the eastern RIS from the new surface low that had progressed towards the West Antarctic Coast, as the IR satellite composite image shows (Fig. 11e). A broad region of cloud cover extended from that surface low over West Antarctica and to the RIS. The AWS pressure observations increased at each site while the trough remained over the western RIS but decreased in spatial extent (Fig. 11f). The 10-m winds remained generally northerly to easterly in the eastern and central RIS, respectively, and remained southerly in the western RIS. The AWS temperature observations were the same or colder than 12 hours prior, as the final warming event ended at Schwerdtfeger.

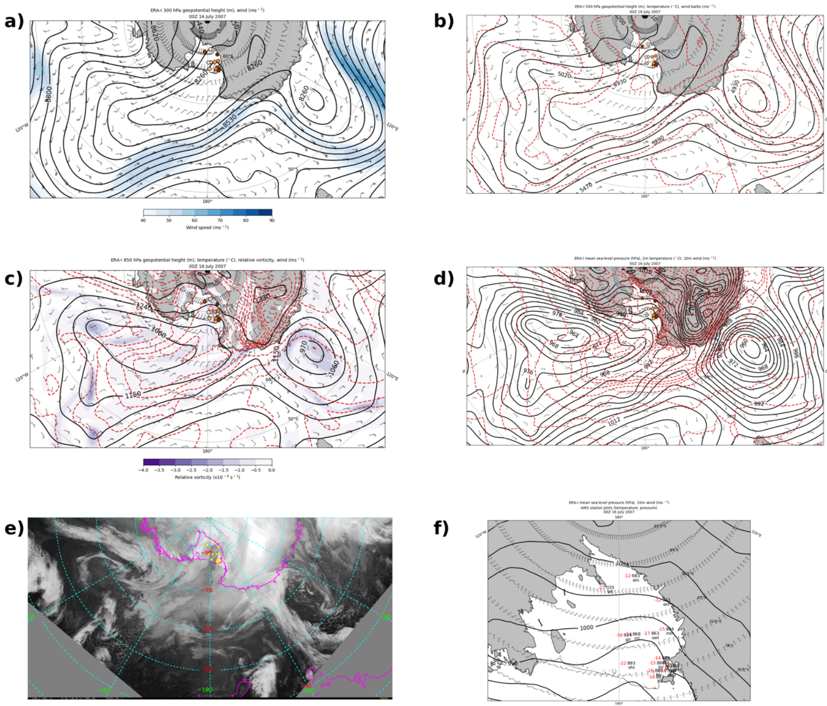

Figure 11: As in Fig. 7 but for 00 UTC 16 July.

4. Discussion

There appear to be four main features that led to the RWEW. The first was a stationary low-ridge setup in the Ross and Amundsen Seas prior to the event. The ERA-Interim

500 hPa 7-11 July composite geopotential height anomalies preceding the RWEW show a pattern resembling a wave train in the Western Hemisphere of the Southern Ocean, with a low-high-low setup extending from the northern Ross Sea, off the coast of West Antarctica, and into the South Atlantic Ocean east of South America, respectively (Fig. 12a). In the Ross Sea, the geopotential height anomaly was more than 150 m below the climatology. The ridge off the coast of West Antarctica was greater than 400 m above the climatology. The strong anomalous 500-hPa ridge in the Amundsen Sea contributed to the northerly surface flow and buildup of anomalously warm 2-m temperatures prior to the RWEW off the West Antarctic Coast while the RIS was free from any major atmospheric disturbances. At the surface, the composite mean sea level pressure field indicates a broad region of low pressure in the northern Ross Sea that was slightly elongated in the north-south direction (Fig. 12b). A broad ridge downstream extended eastward along the West Antarctic Coast, where the warmest 2-m temperature anomalies were located. Between the low pressure and ridge, the orientation of the composite 10-m wind barbs shows near-surface northerly flow.

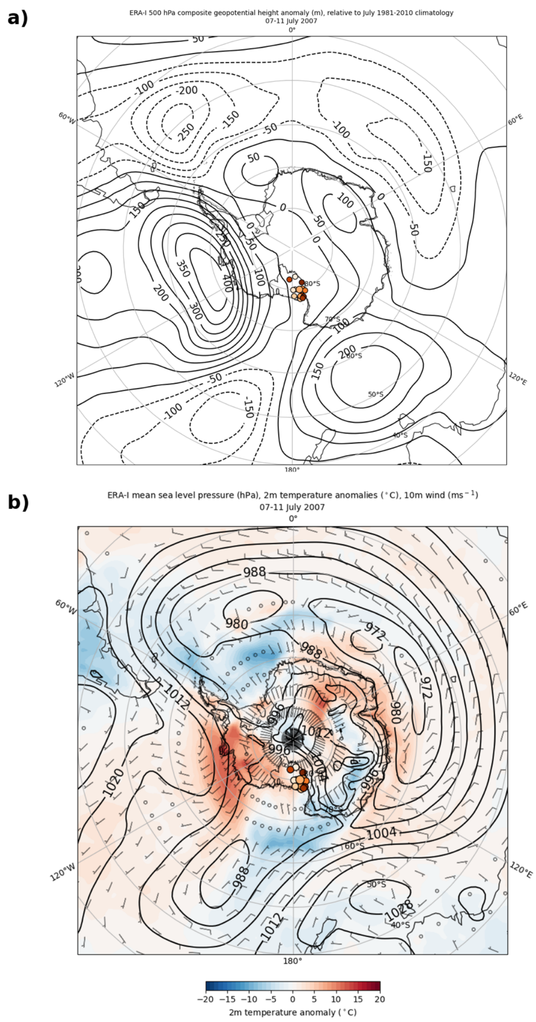

Figure 12: ERA-I composite plots from 07-11 July 2007 of a) 500-hPa geopotential height anomalies (m) (black contours, every 50 m, with negative values dashed); b) mean sea level pressure (hPa) (black contours), 2-m temperature anomalies (° C) (color fill), wind barbs (m s^{-1}). Anomalies are relative to the July 1981-2010 climatology. For a) and b), AWS are plotted as in Fig. 5a.

The second feature was a cold pool that developed over the RIS before the event started, manifested by calm winds and a strong surface inversion and contributing to the establishment of a strong baroclinic zone north of the RIS. The cloud structures varied between the Ross and Amundsen Seas and the RIS two days prior to the beginning of the RWEW, with fog over the open ocean to the north and thin, low clouds to the south over the RIS, both separated by a deep cloud layer. The CloudSat/CALIPSO satellite data retrieval at 09:38:49 UTC 10 July shows the A-train swath extending from 63° S to 81.3° S from the Amundsen Sea, where the ridge was located, southwest over the RIS and over the East Antarctic Plateau (Fig. 13a). The cloud phase data retrieval indicates liquid and mixed phase fog and cloud cover in the lowest ~2 km of the atmosphere in the northernmost portion of the retrieval (Fig. 13b, panel b), between points A and B, over open ocean water (Fig. 13b, panel f). There was a correspondingly strong downwelling longwave radiation (DLR) (Fig. 13b, panel c). The warmest ECMWF temperatures of ~270 K were in this location, nearest the surface. A high-altitude ice cloud layer at ~10 km was in the region as well, which can also be seen in lighter grays and white colors in the infrared composite satellite imagery (Fig. 14), indicating cold cloud tops, from point A southwestward past point C. Over the RIS between points D and E, the low cloud cover thinned even more, as indicated by a smaller region of predominantly ice phase clouds, lower DLR, reflectivity (Fig. 13b, panel a), and lower bottom of the atmosphere longwave cloud radiative effect (BOACRE) values (Fig. 13b, panel e) than between points A and C. While the 5-day composite 2-m temperature anomalies over the RIS indicated only slightly warm anomalies for this period, the hourly AWS temperature observations (Fig. 15) indicate general cooling trends at each location in the two days leading up to the warming events. For most AWS, temperatures trended from near to slightly above the July climatological mean to at least one standard deviation cooler than the mean when the warming event began. In general, wind speeds were calmer in the days leading up to the warming event than during the event (Fig. 15).

With calm winds, minimal cloud cover as the CloudSat/CALIPSO observations indicate, and no insolation since this is in the middle of austral winter, strong surface temperature inversions developed across the RIS. The 06 UTC 12 July vertical temperature profile at Elaine, the AWS to first begin observing warming, is indicative of this strong inversion (Fig. 16). This vertical temperature profile was 10 minutes before the beginning of warming at Elaine, and it shows the steep increase in temperature from the surface to ~975 hPa, followed by a gradual decrease in temperature up to 400 hPa. The ERA-I temperature at 1002 hPa (the surface) was -45.1° C, and at 975 hPa (233 m) it was -28.3° C, a difference of 16.8° C. The magnitude of the warming, according to the Elaine AWS observations, was 39.3° C. Since this is greater than the magnitude of the temperature inversion, this suggests that mixing out of the surface inversion alone would not have been enough to account for all the warming observed.

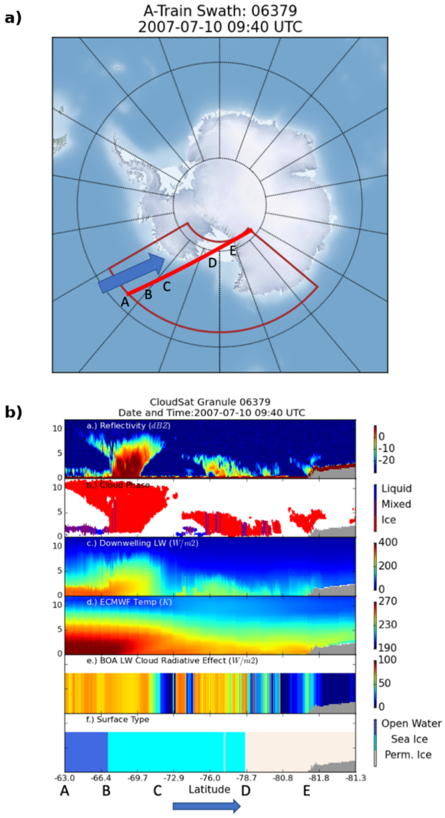

Figure 13: CloudSat/CALIPSO A-train satellite constellation data retrievals at 09:40 UTC 10 July 2007. a) The path of the A-train satellite constellation (red) with the blue arrow denoting the direction of travel. Letters correspond to locations discussed in text. b) Panel a) reflectivity (dBZ) from 0 to -30 dBZ; b) Cloud phase: liquid (blue), mixed (purple), ice (red); c) Downwelling longwave radiation (W m^{-2}) from 0 to 400 W m^{-2}; d) ECMWF temperature (K) from 190 to 270 K; e) bottom-of-atmosphere longwave cloud radiative effect (W m^{-2}) from 0 to 100 W m^{-2}; f) surface type: open water (dark blue), sea ice (light blue), and permanent ice (white). Blue arrow and letters A through E at the bottom correspond to a). The time denotes the time the satellites were at the midpoint of the red line in a).

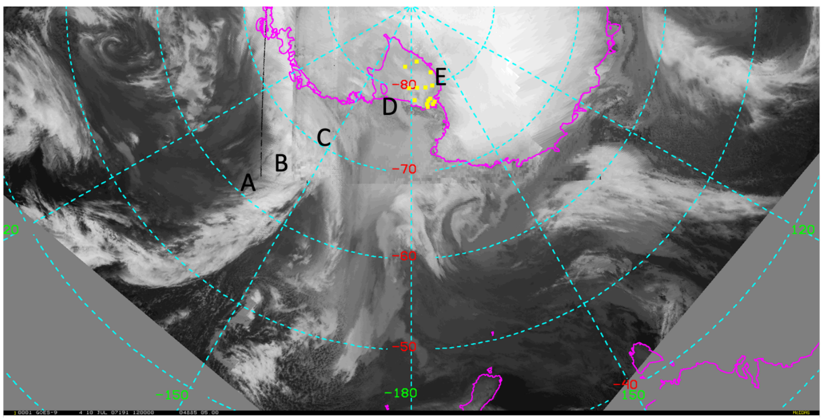

Figure 14: Infrared satellite composite image with annotated letters corresponding to locations in Fig. 13 and yellow dots denoting AWS locations.

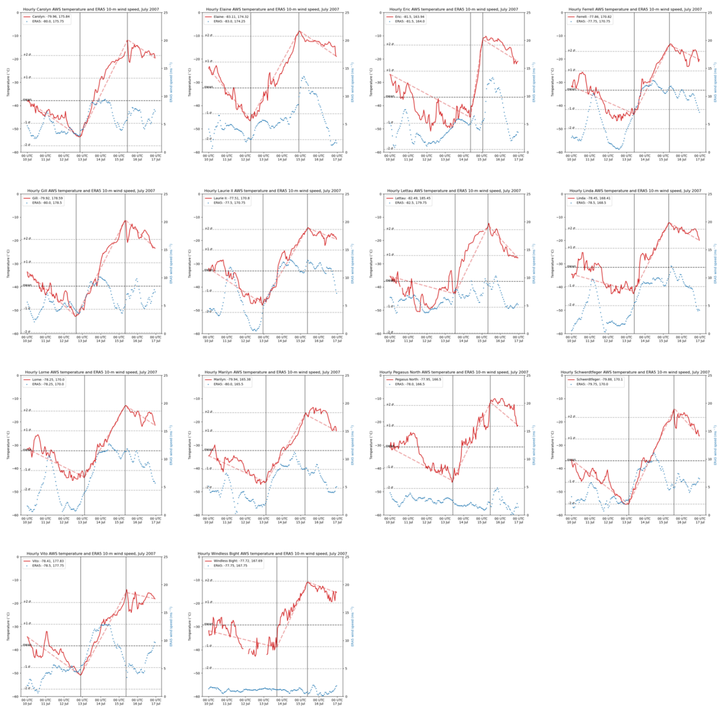

Figure 15: As in Fig. 4, except blue dots are ERA5 10-m wind speeds (m s-1), and dashed red lines denote the temperature trend before, during, and after each respective warming event.

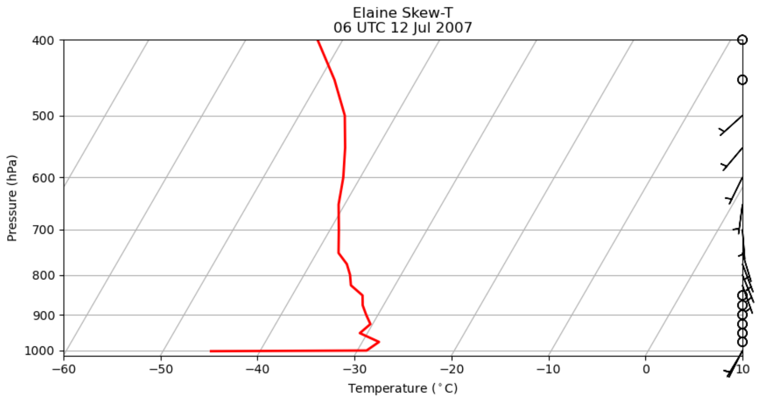

Figure 16: ERA-I 06 UTC 12 July 2007 vertical temperature (° C) profile (solid red line) versus pressure (hPa, note the logarithmic scale) and wind barbs (m s-1) at the grid point nearest Elaine (-83.16°, 174.38°).

The third feature was the eastward progression of a cyclone off the Adelie Land Coast that merged with the existing stationary low in the Ross Sea. Approximately one and a half days before the beginning of the warming event, at 00 UTC 11 July, a surface trough upstream of the Adelie Land Coast progressed southeastward and strengthened into a cyclone off the Adelie Land Coast (Fig. 17). This disturbance had strong upper-level support, as the 00 UTC 11 July 300- and 500-hPa geopotential heights indicated a deep collocated trough and the 850-hPa geopotential heights indicated a closed-off circulation (not shown). The 850-hPa relative vorticity minimum was much stronger at this time than prior minima in this region in the days beforehand, indicating a well-developed cyclone (not shown). While this disturbance progressed eastward off Cape Adare and weakened as it entered the Ross Sea by 12 UTC 12 July (Fig. 8), the deeper barotropic support appeared to provide enough energy for it to shift the Ross Sea cyclone southward. This acted to reorient the baroclinic zone meridionally in the southern Ross Sea as the warm front of the Ross Sea cyclone progressed towards the RIS.

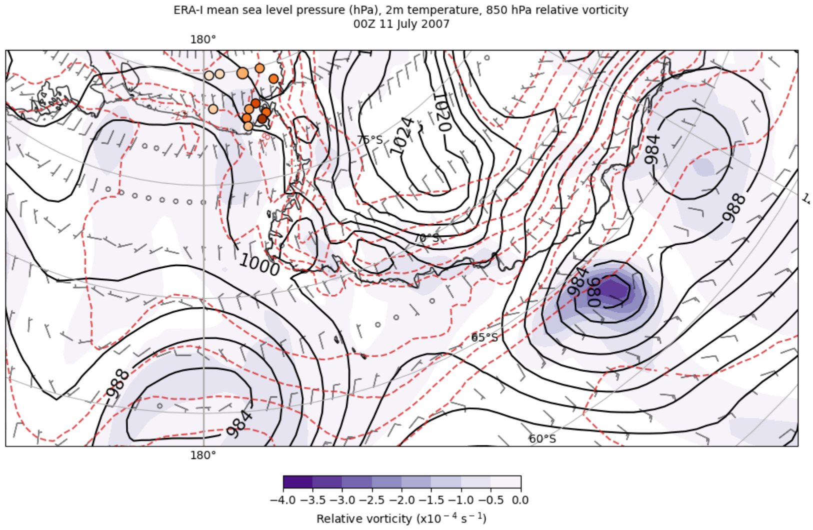

Figure 17: ERA-I 00 UTC 11 July 2007 mean sea level pressure (hPa) (black contours), 2-m temperature (° C) (dashed red contours, 850-hPa relative vorticity (10^{-4} s^{-1}) (fill contours from -4 to 0 every 0.5), and 10-m wind barbs (m s^{-1}). AWS are plotted as in Fig. 5a.

The fourth feature contributing to this warming event was the progression of the warm front associated with this cyclone across the RIS, leading to warm air advection, increased cloud cover, and increased wind speeds. A front is characterized as an area with larger-than-background horizontal temperature gradients, larger-than-background relative vorticity, and larger-than-background static stability [26]. As discussed in Section 3, there was a strong horizontal temperature gradient that extended from the surface to 500 hPa and was established north of the RIS preceding the RWEW. On 12 July, when the surface low in the Ross Sea progressed southward towards the RIS, this region of strong temperature contrast began to move across the RIS and was coincident with a local maximum in cyclonic relative vorticity. Figure 18 shows the 850-hPa temperature gradient and local minimum in cyclonic relative vorticity associated with the warm frontal passage at 850 hPa across the RIS at 12 UTC 14 July. The region of strongest horizontal temperature gradient over the RIS is collocated and just west, or ahead, of the region of strongest relative vorticity and the trough in geopotential heights. In these terms, the warm front was strongest in the northern RIS, closer to the surface cyclone, compared to the southern RIS at Elaine.

The warm frontal signature, however, is still readily evident in the static stability reaching as far south as Elaine. A time-height cross section of ERA5 temperatures at Elaine from 11 July through 16 July illustrates the region of high static stability associated with this warm front (Fig. 19). The black vertical lines denote the beginning (06:10 UTC 12 July) and ending (22:10 UTC 14 July) of the warming event observed at Elaine. From 00 UTC 11 July through approximately 06 UTC 12 July, the atmosphere at Elaine from the surface to 400 hPa was well stratified, as indicated by the nearly constant and horizontally oriented isotherms throughout the atmospheric column. After 06 UTC 12 July, the isotherms in the lowest portion of the atmosphere began sloping towards the surface, indicating warming. Between 06 UTC 12 July and 12 UTC 13 July, the isotherms farther and farther up the atmosphere to 400 hPa began sloping towards the surface, showing warming occurred in more and more of the atmospheric column at Elaine. The sloping bundle of isotherms marks a region of high static stability, the third characteristic feature of a frontal zone, indicating the presence of a warm frontal passage during this RWEW. The ERA-I 00 UTC 15 July vertical temperature profile at Elaine (Fig. 20), just after the warming event ended, also shows warming occurred throughout the atmosphere from the surface to ~400 hPa.

The ERA-I temperature at 981 hPa (the surface) warmed from -45.1° C to -12.9° C, an increase of 32.2° C. At 975 hPa (87 m) it warmed from -28.3° C to -8.5° C, an increase of 19.8° C. The magnitude of the surface inversion from the surface to 975 hPa greatly decreased to 4.4° C. Additionally, the wind barbs indicate increased wind speeds at Elaine throughout the entire column. Wind directions ranged from southeasterly at the surface to east-northeasterly at 400 hPa (backing with height), indicative of warm air advection in the Southern Hemisphere. Given this warm frontal signature is evident in the vertical temperature profile at Elaine and the warm frontal signature at 850 hPa is even more pronounced towards the northern RIS, it can be presumed that an equal or greater magnitude warm frontal signature occurred with this RWEW.

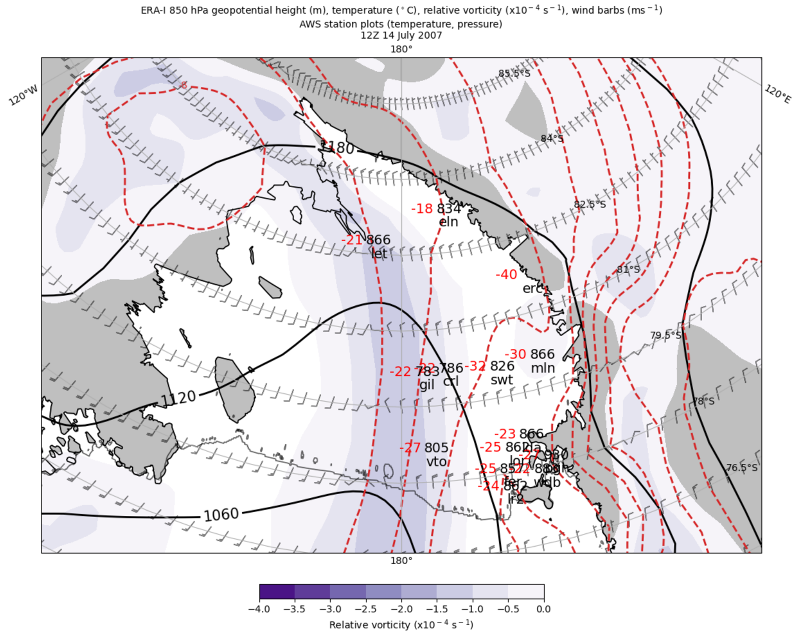

Figure 18: ERA-I 12 UTC 14 July geopotential height (m) (black contours), temperature (° C) (dashed red contours), relative vorticity (10^{-4} s^{-1}) (fill contours from -4 to 0 every 0.5), and wind barbs (m s^{-1}).

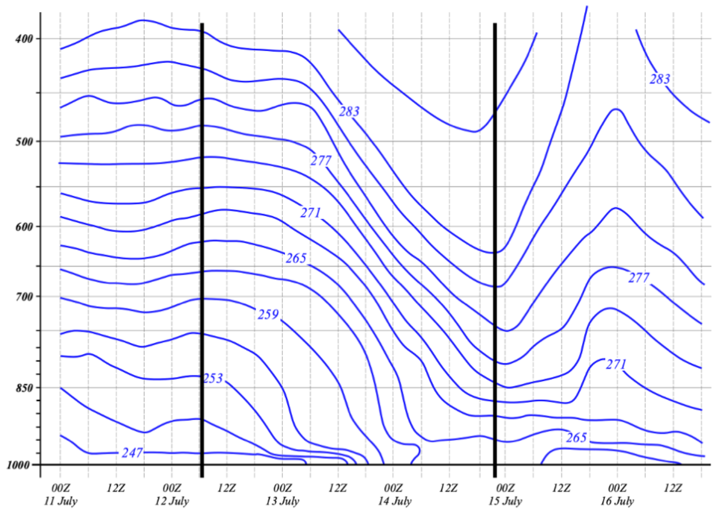

Figure 19: ERA5 time versus pressure (hPa, note the logarithmic scale) of temperature (K) (blue contours) at the grid point nearest Elaine. Black vertical lines denote beginning and ending of warming event.

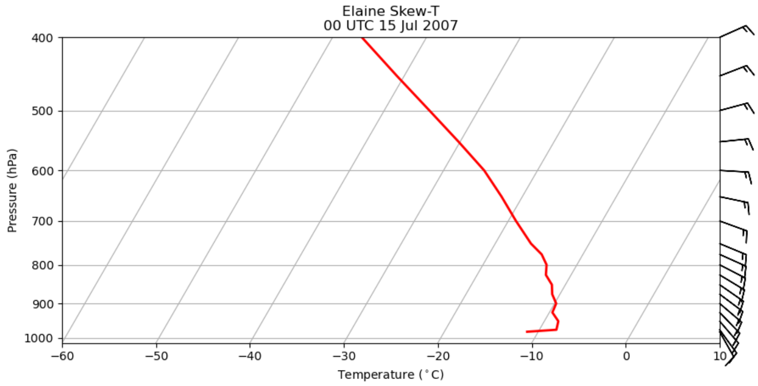

Figure 20: As in Fig. 16 but for 00 UTC 15 July 2007.

The increased wind speeds and variability in wind speed behavior across the RIS may suggest varying mechanisms contributed to the RWEW, including an increase in wind speed over the RIS. Comparing the wind speeds at Elaine (southern RIS) and Vito (northern RIS), an increase in 10-m winds at both locations coincided with the beginning of the warming (Fig. 15). This is consistent with the approach and passage of the warm front; the increased cyclonic vorticity characteristic of the front led to increased wind speeds and warming temperatures. Once the front passed, 10-m wind speeds plateaued at both locations in the middle of the warming, suggesting that a combination of warm air advection and turbulent mixing out of the surface inversion contributed to the beginning of the RWEW. The cloud cover and its longwave radiative feedback further contributed to, and may have sustained, the warming for the latter half of the RWEW as the wind speeds plateaued, though warm air advection was not precluded from continuing in the face of constant wind speeds. Towards the end of the RWEW, at Elaine, wind speeds increased, reaching a maximum after the warming event ended. At Vito, wind speeds decreased towards the end of the event. This suggests that the approaching cyclone in the Ross Sea amplified the Ross Air Stream (RAS) [13-14], a climatological wind regime observed along the Transantarctic Mountains and originating near Elaine.

The wind direction observations at most AWS were more constant compared to their respective climatological means. Figure 21 shows Schwerdtfeger wind observations, comparing those during its warming event (Fig. 21a) to its July 1991-2020 climatology (Fig. 21b). During its warming event, while the prevalent wind direction (west-southwest) did not change, a much larger percentage of wind observations (~70%) were from that direction compared to the climatology (~22%). As discussed in Section 2, synoptic-scale cyclones were found to enhance the RAS by increasing the pressure gradient. As shown in Section 3, the mean sea level pressure gradient over the RIS was weak before the RWEW, and it increased as the cyclone approached and the warm front progressed across the RIS (Figs. 7f-11f). The RAS has been found to be most prevalent during winter months, and it may be that its enhancement and sustenance occurs in conjunction with rapid surface warming events such as this RWEW.

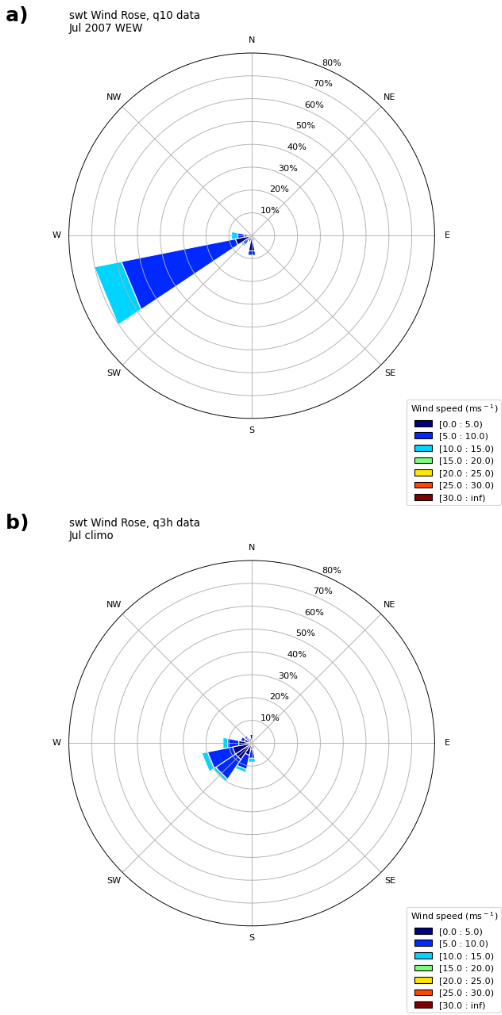

Figure 21: Schwerdtfeger wind rose plots a) during the warming event and b) for its July 1991-2020 climatology.

5. Conclusions

This study investigated a Regional Warming Event in Winter (RWEW) that occurred from 12-15 July 2007 and was observed by the University of Wisconsin-Madison (UW-Madison) Automatic Weather Station (AWS) network. A total of 14 AWS observed warming during this RWEW, with the first AWS (Elaine) observing warming at 06:10 UTC 12 July and the last warming ending at Schwerdtfeger at 13:50 UTC 15 July. Using ERA-Interim and ERA5 reanalysis data, satellite composite imagery, CloudSat/CALIPSO satellite data retrievals, and AWS observations, this study investigated the synoptic-scale setup preceding, during, and after the RWEW to determine the large-scale meteorological factors that led to the RWEW. It was found that the passage of a warm front across the RIS from an approaching cyclone in the Ross Sea eroded the cold pool that developed over the RIS and led to the RWEW.

In the days leading up to the RWEW, a 500-hPa wave-train pattern of a geopotential height minimum in the northern Ross Sea and a ridge downstream in the Amundsen Sea led to persistent, northerly flow and buildup of anomalously warm 2-m temperatures off the coast of West Antarctica, north of the RIS. The location of the associated surface cyclone in the northern Ross Sea was a typical positioning of the climatological low known as the Amundsen Sea Low (or Amundsen-Bellingshausen Seas Low) [27, 10]. Over the RIS, calm atmospheric conditions and minimal cloud cover led to the development of a cold pool, with AWS temperatures cooling to greater than one standard deviation below their climatological means. Strong surface temperature inversions occurred, with some inversions reaching 20° C from the surface to 975 hPa. A strong baroclinic zone developed off the West Antarctic Coast between the regions of warm and cold air. Upstream of the Ross Sea cyclone, two cyclones developed off the Adelie Land Coast, a region with known cyclogenesis [12], and progressed eastward. The first cyclone had minimal upper-level support and weakened as it entered the Ross Sea. The second cyclone had more substantial upper-level support. It maintained its strength for longer as it progressed eastward into the Ross Sea. It merged with the stationary Ross Sea cyclone, after which the Ross Sea cyclone strengthened and progressed southward towards the RIS. A warm front then developed on the southern portion of the cyclone, with the pre-established baroclinic zone progressing across the RIS from east to west. The RWEW began shortly after the merging of the two cyclones in the Ross Sea, as the progression of the warm front brought with it increased winds and cloud cover over the RIS.

The mechanisms for surface warming were investigated. The warm frontal signature was found to reach as far south as Elaine, spanning the entire RIS. Turbulent mixing, warm air advection, and longwave radiative heating due to cloud cover, acting in concert, were the culprits in generating surface warming of this magnitude. One important finding was that the strength of the surface inversions leading up to the RWEW did not exceed 30° C. Therefore, mixing out of the surface inversion alone could not account for all the warming observed in the RWEW. It is likely, however, that turbulent mixing played some role. It was found that, at most AWS, the beginning of the warming event coincided with increasing wind speeds. This suggests some combination of warm air advection and turbulent mixing could have initiated the warming. Cloud cover, however, accompanied the warm front and contributed to an increase in longwave radiation at the surface. This may have contributed to the onset of warming and sustained the warming throughout the event. As the RWEW continued over the RIS, wind speeds at sites in the northern RIS plateaued and decreased while wind speeds at sites in the southern RIS plateaued and increased. This wind pattern also resembles the climatological wind regime over the RIS [7], with weaker winds in the northern RIS and stronger winds along the Transantarctic Mountains. It is also indicative of the nearby surface cyclone, in turn enhancing the Ross Air Stream (RAS), a climatological wind regime of strong southerly winds along the Transantarctic Mountains [11, 13-14].

Future work on this RWEW will investigate how the 500-hPa wave train pattern was established prior to the warming, focusing on tropical teleconnections. Additionally, a more quantitative analysis can better characterize the different warming mechanisms over the RIS, investigating how the increased wind speeds impact the magnitude of warm air advection and turbulent mixing over the RIS. With an enhanced RAS, adiabatic warming due to compression from katabatic winds off the West and East Antarctic Plateaus may also contribute to warming at AWS along the Transantarctic Mountains. [28] did a case study of barrier wind corner jet formation in the southern RIS during which surface wind speeds and temperatures increased rapidly, using AWS data and AMPS output to show how several forcing mechanisms, including an upper-level ridge and a surface mesocyclone, induced such an event. The surface energy budget can be further investigated and quantified to determine the magnitude of the longwave radiative feedback due to the cloud cover over the RIS, including the possible latent heat release due to cloud formation. The variation of these warming mechanisms across the RIS may be useful to show how likely such strong and rapid warming events are to occur in the future. This may also provide insights into extreme departures from climatology in austral winter that sometimes occur over other regions in Antarctica.

Author Contributions: Conceptualization, D. M., J. M., L. K., and M. L.; methodology, D. M., J. M., L. K., and M. L.; validation, D. M., J. M., L. K., and M. L.; formal analysis, D. M., J. M., L. K., and M. L; investigation, D. M., J. M., L. K., and M. L; resources, D. M., J. M., L. K., and M. L; data curation, D. M., J. M., and L. K.; writing—original draft preparation, D. M.; writing—review and editing, D.

M., J. M., L. K., and M. L.; visualization, D. M., J. M., L. K., and M. L.; supervision, J. M., L. K., and M. L; project administration, M. L. and J. M.; funding acquisition, M. L..

Funding: This research was funded by the National Science Foundation, grant number 1543305 and 1924730.

Institutional Review Board Statement: Not applicable.

Informed Consent Statement: Not applicable.

Data Availability Statement: The data presented in this study are openly available in amrdcdata.ssec.wisc.edu/<link>, at <DOI> <reference number>. (The data used in this study will soon have an entry in this repository, including a DOI.)

Acknowledgments: Not applicable.

Conflicts of Interest: The authors declare no conflict of interest. The funders had no role in the design of the study; in the collection, analyses, or interpretation of data; in the writing of the manuscript; or in the decision to publish the results.

Appendix A

Not applicable.

Appendix B

Not applicable.

References

1. Lazzara, M., Weidner, G., Keller, L., Thom, J., Cassano, J. Antarctic Automatic Weather Station Program: 30 Years of Polar Observation. *Bull. Amer. Meteor. Soc.* **2012a**, *93*, 1519-1537.
2. van Loon, H. The Half-Yearly Oscillations in Middle and High Southern Latitudes and the Coreless Winter. *J. Atmos. Sci.* **1967**, 24, 472-486. DOI:10.1175/1520-0496(1967)024<0472:THYOIM>2.0.CO;2.
3. Thompson, D. The coreless winter at Scott Base, Antarctica. *Quart. J. R. Met. Soc.* **1969**, *95*, 404-407.
4. Schwerdtfeger, W. Chapter 4. In The Climate of the Antarctic; Orvig, S., Ed.; World Survey of Climatology: Elsevier, Amsterdam, 1970; Volume 14, pp. 253–355.
5. Wendler, G., Kodama, Y. The kernlose winter in Adelie Coast. *Antarctic Meteorology and Climatology: Studies Based on Automatic Weather Stations (eds D. H. Bromwich and C. R. Stearns) American Geophysical Union, Washington, D.C.* **1993**, *61*, 139-147. DOI:10.1029/AR061p0139.
6. Lazzara, M. A., Keller, L. M., Markle, T., Gallagher, J. Fifty-year Amundsen-Scott South Pole station surface climatology. *Atmos. Res.* **2012b**, *118*, 240–259. DOI: 10.1016/j.atmosres.2012.06.027.
7. Costanza, C., Lazzara M., Keller, L., Cassano, J. The surface climatology of the Ross Ice Shelf Antarctica. *Int. J. Climatol.* **2016**, *36*, 4929-4941.
8. Hirasawa, N., Hisashi, N., Yamanouchi, T. Abrupt changes in meteorological conditions observed at an inland Antarctic station in association with wintertime blocking. *Geophys. Res. Lett.* **2000**, *27*, 1911-1914.
9. Hirasawa, N., Nakamura, H., Motoyama, H., Hayashi, M., Yamanouchi, T. The role of synoptic-scale features and advection in prolonged warming and generation of different forms of precipitation at Dome Fuji station, Antarctica, following a prominent blocking event. *J. Geophys. Res. Atmos.* **2013**, *118*, 6916-6928. DOI:10.1002/jgrd.50532.
10. Hosking, J. S., Orr, A., Marshall, G. J., Turner, J., Phillips, T. The influence of the Amundsen-Bellingshausen Seas Low on the climate of West Antarctica and its representation in coupled climate model simulations. *J. Climate* **2013**, *26*, 6633-6648. DOI:10.1175/JCLI-D-12-00813.1.
11. Coggins, J. H., McDonald, A. J., Jolly, B. Synoptic climatology of the Ross Ice Shelf and Ross Sea Region of Antarctica: *k*-means clustering and validation. *Int. J. Climatol.* **2014**, *34*, 2330-2348. DOI:10.1002/joc.3842.
12. Bromwich, D. H., Steinhoff, D. F., Simmonds, I., Keay, K., Fogt, R. L. Climatological aspects of cyclogenesis near Adelie Land, Antarctica. *Tellus A: Dynamic Meteorology and Oceanography* **2011**, *63:5*, 921-938. DOI: 10.1111/j.1600-0870.2011.00537.x
13. Parish, T.R., Cassano, J. J., Seefeldt, M. W. Characteristics of the Ross Ice Shelf air stream as depicted in Antarctic Mesoscale Prediction System simulations. *J. Geophys. Res. Atmos.* **2006**, *111(D12)*. DOI: 10.1029/2005JD006185.
14. Seefeldt, M. W., Cassano, J. J. An Analysis of Low-Level Jets in the Greater Ross Ice Shelf Region Based on Numerical Simulations. *Mon. Wea. Rev.* **2008**, *136*, 4188-4205. DOI:10.1175/2008MWR2455.1.

15. Seefeldt, M. W., Cassano, J. J. A description of the Ross Ice Shelf air stream (RAS) through the use of self-organizing maps (SOMs). *J. Geophys. Res. Atmos.* **2012**, *117(D09)*. DOI: 10.1029/2011JD016857.
16. Dee, D. P., and Coauthors The ERA-Interim reanalysis: configuration and performance of the data assimilation system. *Q.J.R. Meteorol. Soc.* **2011**, *137*, 553–597. DOI:10.1002/qj.828.
17. Hersback, H., and Coauthors The ERA5 global reanalysis. *Quart. J. Roy. Meteor. Soc.* **2020**, *146*, 1999-2049. DOI: https://doi.org/10.1002/qj.3803.
18. Tetzner, D., Thomas, E. R., Allen, C. S. A validation of ERA5 reanalysis data in the southern Antarctic Peninsula-Ellsworth Land region, and its implications for ice core studies. *Geosciences* **2019**, *9*, 289. DOI: 10.3390/geosciences9070289.
19. Kohrs, R., Lazzara, M., Robaidek, J., Santek, D., Knuth, S. Global Satellite Composites – 20 Years of Evolution. *J. Atmos. Res.* **2014**, *135-136*, 8-34. DOI:10.1016/j.atmosres.2013.07.023.
20. Lazzara, M. A., Benson, J. M., Fox, R. J., Laitsch, D. J., Rueden, J. P., Santek, D. A., Wade, D. M, Whittaker, T. M., Young, J. T. The man computer interactive data access system: 25 years of interactive processing. *Bull. Amer. Meteor. Soc.* **1999**, *80*, 271-284. DOI:10.1175/1520-0477(1999)080<0271:TMCIDA>2.0.CO;2.
21. L'Ecuyer, T. S., Jiang, J. H. Touring the atmosphere aboard the A-Train. *Phys. Today* **2010**, *63*, 36–41. DOI:10.1063/1.3463626.
22. Marchand, R., Mace, G. G., Ackerman, T., Stephens, G. Hydrometeor detection using Cloudsat – An earth-orbiting 94-GHz cloud radar. *J. Atmos. Oceanic Tech.* **2008**, *25*, 519–533. DOI: https://doi.org/10.1175/2007JTECHA1006.1.
23. Wang, Z., Vane, D., Stephens, G. Level 2 Combined Radar and Lidar Cloud Scenario Classification Product Process Description and Interface Control Document, NASA JPL CloudSat project document Version 1.0; **2012**, pp. 61.
24. Henderson, D. S., L'Ecuyer, T., Stephens, G., Partain, P., Sekiguchi, M. A multisensory perspective on the radiative impacts of clouds and aerosols. *J. Appl. Meteor.* **2013**, *52*, 853–871. DOI: https://doi.org/10.1175/JAMC-D-12-025.1.
25. CloudSat Data Processing Center (DPC). Available online: https://www.cloudsat.cira.colostate.edu/data-products/ecmwf-aux (Accessed on 31-03-2022).
26. Martin, J. E. Mid-Latitude Atmospheric Dynamics: a first course. **2006**.
27. Turner, J., Phillips, T., Hosking, J. S., Marshall, G., Orr, A. The Amundsen Sea Low. *Int. J. Climatol.* **2013**, *33*, 1818-1829. DOI: 10.1002/joc.3558.
28. Nigro, M., Cassano, J. J., Lazzara, M. A., Keller, L. M. Case Study of a Barrier Wind Corner Jet off the Coast of the Prince Olav Mountains, Antarctica. *Mon. Wea. Rev.* **2012,** *140*, 2044-2063. DOI: https://doi.org/10.1175/MWR-D-11-00261.1.